JGR Solid Earth

RESEARCH ARTICLE

Key Points:
- A comprehensive stress drop distribution for the Iquique Earthquake rupture region is computed using a spectral ratio approach
- The stress drops estimates reveal no large scale pattern or major trend such as a depth dependency
- We describe minor stress drop variations in greater detail and find a relatively strong scaling with moment for the entire data set

Correspondence to:
J. Folesky,
jonas.folesky@geophysik.fu-berlin.de

Stress Drop Variations in the Region of the 2014 M_W8.1 Iquique Earthquake, Northern Chile

Jonas Folesky[1] , **Jörn Kummerow[1]**, and **Serge A. Shapiro[1]**

[1]Department of Geophysics, Freie Universität Berlin, Berlin, Germany

Abstract We compute stress drops from *P* and *S* phase spectra for 534 earthquakes in the source region of the 2014 M_w8.1 Iquique megathrust earthquake in the northern Chilean subduction zone. An empirical Green's function based method is applied to suitable event pairs selected by template matching of eight years of continuous waveform data. We evaluate the parameters involved in the stress drop estimation, consider the effect of the local velocity structure and apply an empirical linear relation between *P* and *S* phase related geometry factors (*k* values). Data redundancy produced by multiple empirical Green's function and the combination of *P* and *S* phase spectra leads to a substantial reduction of uncertainty and robust stress drop estimates. The resulting stress drop values show a well-defined log-normal distribution with a median value of 4.36 MPa; most values range between 0.1 and 100 MPa. There is no evidence for systematic large scale lateral variations of stress drop. A detailed analysis reveals several regions of increased median stress drop, an increase with distance to the interface, but no consistent increase with depth. This suggests that fault regime and fault strength have a stronger impact on the stress drop behavior than absolute stresses. Interestingly, we find a weak time-dependence of the median stress drop, with an increase immediately before the April 1, 2014 M_w8.1 Iquique mainshock, a continuous reduction thereafter and a subsequent recovery to average values. Additionally, the data set indicates a relatively strong dependence of stress drop on magnitude which extends over the entire analyzed magnitude range.

1. Introduction

Stress drop relates the rupture dimension to the seismic moment of earthquakes which makes it a central parameter of earthquake source analysis, having both practical implications, for example, on high frequency-ground motion, and theoretical ones on the rupture processes of earthquakes in general. The complex nature of earthquake rupture and with it the behavior of stress drop still raise important questions which have not yet been answered conclusively.

Stress drop has been observed to depend on different factors such as depth, stress conditions and tectonic setting (e.g., Allmann & Shearer, 2009; Boyd et al., 2017; Kanamori & Anderson, 1975; Sibson, 1974; Uchide et al., 2014; Venkataraman & Kanamori, 2004). Results, however, are not always univocal. For example, Venkataraman and Kanamori (2004) and Uchide et al. (2014) report strong dependence on earthquake depth, while Allmann and Shearer (2009) find evidence for a weak depth dependence with some variability depending on example, region or faulting type. Similarly, multiple studies support the self-similarity of the rupture process, which suggests constant stress drop independent of event magnitude (e.g., Abercrombie, 1995; Allmann & Shearer, 2009; Shearer et al., 2006), but more recent studies also report a considerable correlation between stress drop and seismic moment for different source regions (e.g., Abercrombie et al., 2016; Trugman & Shearer, 2017).

The interpretation of results is generally complicated by the inherent problem that individual stress drop estimates often scatter heavily for a given study area, and different techniques and models produce significant variability of stress drop estimates. Even for similar approaches, the parameter choice may introduce systematic changes of the resulting stress drop values. Therefore, at least for comparative studies, it is beneficial when stress drops are calculated in a consistent way for a large number of earthquakes, as applied in Shearer et al. (2006) or Allmann and Shearer (2009).

For large data sets with predominantly small to medium-sized earthquakes, one practical way to compute stress drops is from the spectra of the recorded seismograms. One popular approach is the spectral

decomposition introduced by Shearer et al. (2006) which uses a global empirical Green's function (EGF) obtained by an iterative stacking procedure. This method was applied both globally (Allmann & Shearer, 2009) and also in more detail to different regions of the world, for example, in California (Goebel et al., 2015; Shearer et al., 2006; Trugman & Shearer, 2017) and in the Japan subduction zone (Uchide et al., 2014).

A second frequently used approach is the spectral ratio technique based on the classical EGF concept (e.g., Frankel, 1982; Mueller, 1985) where individual, well selected partner events are used to clean the earthquake spectrum from contributions of raypath and site response. Different realizations have been applied over the years to a variety of data sets, including borehole, local and regional recordings (Abercrombie, 2014; Abercrombie et al., 2016; Hutchings & Viegas, 2012). Both approaches were compared in a recent study by Shearer et al. (2019) which concludes that results are comparable if additional constraints on the corner frequencies of the smaller event in the spectral ratios are introduced. The authors emphasize, however, that the most reliable results are achievable by uniform processing of comprehensive data sets which approves the subsequent interpretation of internal variations. In this study, we follow this guideline.

We study here seismicity in the northern Chilean subduction zone, a region, which experienced two megathrust earthquakes in recent years, the 2007 M_W7.7 Tocopilla event and the 2014 M_W8.1 Iquique event. Despite the occurrence of these two megathrust earthquakes the postulated northern Chilean seismic gap still remains partially unbroken (Hayes et al., 2014; Schurr et al., 2014), and therefore is of great interest. The study area has been monitored intensively since 2006 by the IPOC network (IPOC, 2006). Recently, a comprehensive earthquake catalog of over 100,000 earthquakes for the time period of 2007–2017 and based on the IPOC seismic station data was published by Sippl et al. (2018). Detailed studies have analyzed various characteristics of the study area such as local seismicity, including the 2007 Tocopilla and 2014 Iquique earthquakes (e.g., Fuenzalida et al., 2013; Hayes et al., 2014; Schurr et al., 2014, 2012), their foreshock and aftershock behavior (Cesca et al., 2016; Hainzl et al., 2019; Ruiz et al., 2014), ground motion and locking in pre-, inter- and post-seismic phases (Hoffmann et al., 2018; Li et al., 2015; Moreno et al., 2018), fluid-migration and velocity ratios (Bloch, John, et al., 2018), event mechanisms (Cesca et al., 2016), and source characteristics such as directivity (Folesky, Kummerow, & Shapiro, 2018) and corner frequency and radiated energy (Derode & Campos, 2019) for selected subsets of events.

One still missing, essential aspect is a comprehensive analysis of stress drop. While the region has been covered by few global stress drop studies which are methodically confined to large earthquakes (Allmann & Shearer, 2009; Ye et al., 2016) the distribution of stress drop for small to medium sized seismicity is still poorly known. Only single studies report for small numbers of particular events in the Iquique region (Derode & Campos, 2019) and in the Tocopilla region (Lancieri et al., 2012).

Simultaneously, the existing data set from northern Chile constitutes an intriguing target because of its long time span, its large spatial extent, the different seismically active units covered (plate interface, upper crust, oceanic crust, and mantle, see Sippl et al., 2018) and in particular the recorded intense seismicity related to the fore- and aftershock series of the 2007 Tocopilla event and the 2014 Iquique event.

In this study, we present a workflow which is adapted to the consistent analysis of stress drops for large data sets by relying on a spectral ratio approach similar to Abercrombie (2014) or Huang et al. (2016). We focus on the particularly rich seismicity data in and around the rupture domain of the 2014 Iquique event (Figure 1). We first describe the method and how we apply it to our data. We discuss the influence of uncertainties and limitations introduced by event station geometry, EGF event selection, signal bandwidth, spectral model used, applied k parameters, seismic velocity model, smoothing, and seismic moment. We complement this evaluation by an analysis of the robustness of the obtained corner frequencies. After this, we study the spatial distribution and temporal variation of stress drop.

2. Catalog and Data

We use in total the 23 seismic broadband stations of the Integrated Plate Boundary Observatory Chile (IPOC). The network extends from north to south over a length of about 700 km between 17.6°S and 24.6°S. This study focuses on the sub-region 19°S–21°S and 69.5°S –71.5°W which is shown in Figure 1 by a green square. Event origin times, P and S arrival time picks and event locations are taken from the catalog by
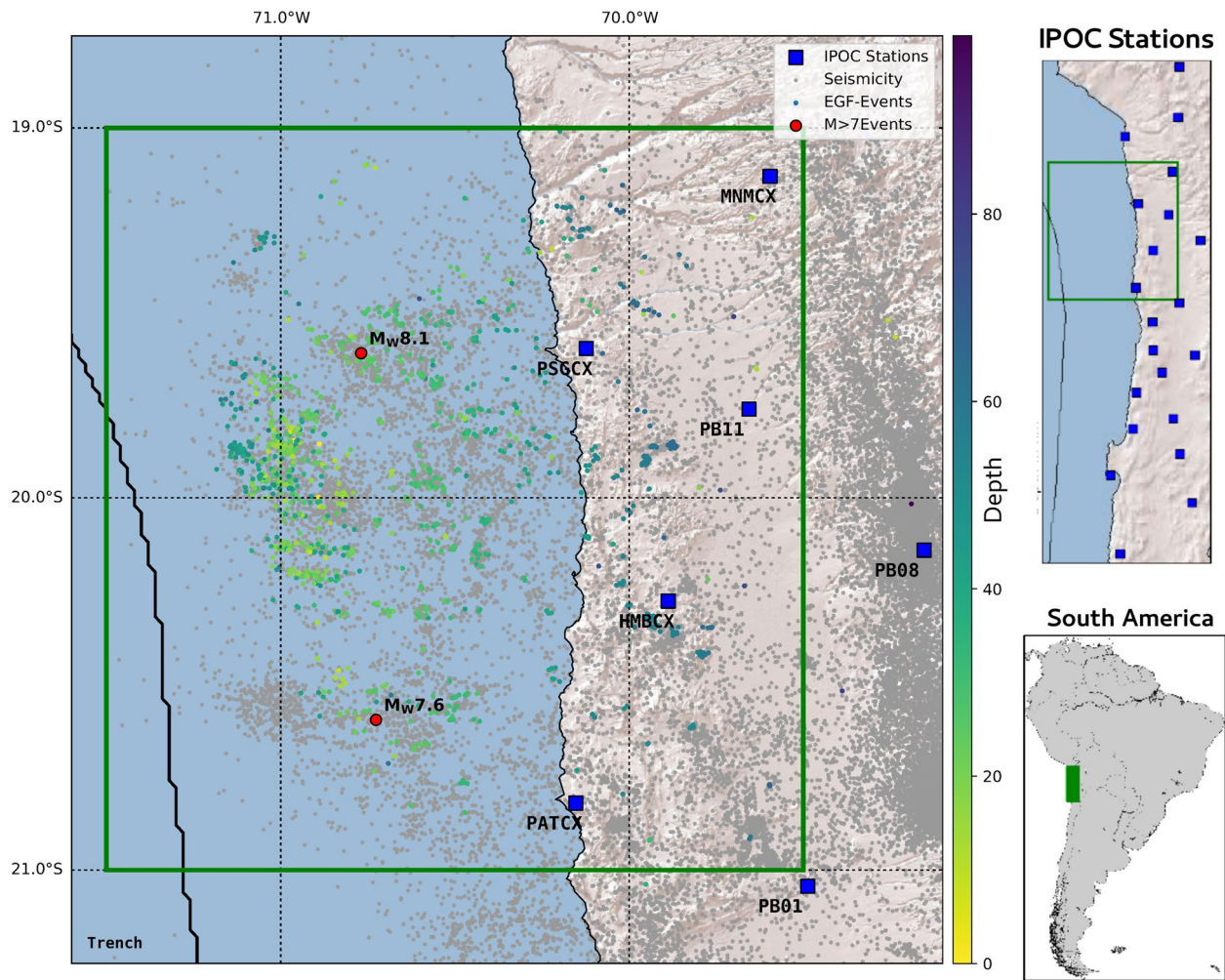
Figure 1. Map of the research area in northern Chile. The 2610 events used in this study are color coded according to their depth. Events from the catalog of Sippl et al. (2018) are underlain in gray. Epicenters of the M_W 8.1 2014 Iquique event and its M_W 7.6 largest aftershock are plotted in red. The IPOC permanent broadband station network (23 stations) are displayed on the upper right.

Sippl et al. (2018) that consists of more than 100,000 double-difference relocated events. The corresponding 100 Hz, three-component waveform data were accessed through the EIDA web service of GFZ Potsdam (Bianchi et al., 2015).

In this region, seismicity occurs mainly on the interface between the subducting oceanic Nazca plate and the overlying South American plate, with some additional events in the overlying continental crust and also in an active deeper band, located about 20–25 km below the interface within the oceanic mantle.

3. Method

We apply an EGF method called the spectral ratio approach, where an EGF is a smaller earthquake with similar location and focal mechanism as the target event. The method can be used to extract detailed source properties of the target event such as source time function or directivity without explicit knowledge of path effects or attenuation (cf. Hutchings & Viegas, 2012, for an overview). We apply an approach that is based on the fit of an appropriate source model to the spectral ratio between target event and EGF event to identify the corner frequency of the larger event from the event pair. The procedure is described in the following.

3.1. Selection of Suitable EGF Pairs

We start the analysis by selecting 9071 catalog events from the earthquake catalog by Sippl et al. (2018) which are located in the study area and which are well recorded by the neighboring IPOC stations. For each catalog event, we perform a template matching scan of the continuous waveform data recorded on the vertical components of the five IPOC stations PB01, PB02, PB08, PB11, and PB12 for the years 2008–2016. A bandpass from 1 to 4 Hz is applied. The templates have a length of 35 s starting 5 s before *P* pick and include both *P* and *S* wave coda. If the normalized cross-correlation coefficient of cc = 0.8 is exceeded at minimum three different stations, the detected and the template event are defined as a potential event pair. The long cross-correlation time window encompassing both the *P* and the *S* phase window ensures the appropriateness of the EGF in terms of co-location and similarity of mechanism of both events (Menke, 1999). Using this procedure, we obtain in total 9,950 event pairs. Most of the EGF events are new detections which were not listed in the catalog before. For further analysis, we also require a minimum magnitude difference of $\Delta M \geq 1$. This is computed from the ratio of the peak amplitude values (velocities) for each target event with its corresponding EGF event at station PB11 where $A_{\text{target}}/A_{\text{EGF}} \geq 10$. After application of this criterion the number of potential events pairs reduces to 2610 which remain for the analysis. Their locations are highlighted in Figure 1.

3.2. Spectral Ratio and Data Fitting

We apply a spectral ratio approach similar to Abercrombie et al. (2016) and Huang et al. (2016) where the spectrum of a target event is divided by the spectrum of its corresponding EGF event. The resulting spectral ratio can be used to assess the corner frequency of the larger and the smaller event as well as the ratio of their seismic moments. In theory, this can be described by the ratio of two events $i = 1, 2$ under the assumption of a specific spectral source model, for example, the one of Brune (1970) or Boatwright (1980):

$$\frac{u_1(f)}{u_2(f)} = \frac{\Omega_1}{\Omega_2} \left(\frac{1 + (f / f_{c_2})^{\gamma n}}{1 + (f / f_{c_1})^{\gamma n}} \right)^{\frac{1}{\gamma}},$$

(1)

where u_i is the displacement, Ω_i is proportional to the seismic moment M_{0i}, f_{ci} is the corner frequency and n the spectral falloff rate while γ depends on the assumed source model (e.g., $\gamma = 1$ for the Brune model, $\gamma = 2$ for the Boatwright model). The latter model of Boatwright (1980) predicts a sharper cornered source spectrum, and when applied to our data we find a consistently lower RMS compared to the model of Brune (1970). Therefore, the subsequent analysis is performed using the Boatwright model with $\gamma = 2$. In principal, it is possible to allow for variations of the falloff rate n, but this would introduce additional uncertainties into the estimation of the corner frequency (Kaneko & Shearer, 2014). To ensure better comparability and to limit the degree of freedom for the fitting (Kaneko & Shearer, 2015), we fix the value to $n = 2$ which matches our data well.

The entire procedure is computed separately for *P* and *S* phases. Data are first detrended and then bandpass filtered between 0.8 and 40 Hz, all using built-in Obspy functions (Beyreuther et al., 2010). We have tested different passbands and we recognize a cutoff at about half the upper corner of the filter as described by Ruhl et al. (2017). Consequently, we have to remove events that potentially have corner frequencies higher than half the upper bandpass corner (i.e., 20 Hz). In this study, we can expect to resolve most events with magnitudes $M > 2.5$ (see Limitations Section and Figures S1 and S2 for further explanation).

For the *P* phases, we select a time window starting at 0.5 s before the *P* phase pick and ending at 1.7 times the catalog based *P* phase travel time, the approximate *S* phase arrival. For the *S* phases, the window is taken relative to this approximate *S* pick with a 1.7 times longer duration. The minimum duration for both time windows are 10 s and 17 s, respectively.

We compute the event spectrum of each individual trace and compare it with the noise spectrum from the time window directly preceding the P phase. Similar to the approach by Shearer et al. (2019), we reject traces with an average SNR of less than three in any of five frequency bands (1.5–5, 5–10, 10–15, 15–20, and 20–25 Hz). This is done for main event and EGF-event. We obtain a single, average spectral ratio by taking

the median of all individual trace spectral ratios for each frequency point. This step is necessary to reduce spherical variation of the source characteristics (here f_c, see e.g., Abercrombie et al., 2017). We require that minimum four traces satisfy the selection criteria in order to accept an event. On average 17 traces contribute to an average ratio. In the next step this spectral ratio is smoothed using the approach of Konno and Ohmachi (1998) which was developed originally to stabilize the spectral ratio between horizontal and vertical components for computing ground motion characteristics. The method ensures a constant number of points in the given frequency bin to mitigate an overweight of high frequencies while smoothing (Huang et al., 2016).

The theoretical spectral ratio model (Equation 1) is then fitted to the smoothed average spectral ratio. We optimize for the parameters f_{c_1}, f_{c_2} and $\Omega_{1/2}$ using the trust region reflective method from scipy curve_fit to describe the shape of the entire spectral ratio. We constrain the corner frequencies as follows: 1 Hz $\leq f_{c_1} < f_{c_2} \leq 50$ Hz. Tests with a fixed fc_2 as proposed by Shearer et al. (2006) and Hardebeck and Aron (2009) produced reasonable fits for many events but also generated some artifacts, especially for events with low corner frequencies f_{c_1}. Additionally, an impact on the absolute value of f_{c_1} was noticed. Hence we do not fix the corner frequency of the smaller event, f_{c_2}. We could not study the variability of f_{c_2} because for most events it may be biased due to the limitations by the available frequency band. For further analysis, we only use f_{c_1}, henceforth denoted as f_c.

3.3. Computation of Stress Drop

To compute the stress drop we take the circular source model as derived by Eshelby (1957) and Madariaga (1976) and write:

$$\Delta\sigma = \frac{7\pi\mu\bar{D}}{16r} = \frac{7M_0}{16r^3},\tag{2}$$

where r is the approximate fault radius, $\bar{D}$ is the average slip on the fault, μ is the shear modulus, and M_0 is the seismic moment. In general, slip and fault dimensions are not easily determined, and we cannot compute the stress drop directly (Kanamori & Anderson, 1975). We, therefore, resort to a method which derives stress drop from the source displacement spectrum. The approach of Brune (1970) provides a link between source radius and the spherically averaged corner frequency (see also Madariaga, 1976; Kaneko & Shearer, 2014, 2015):

$$f_c = k\frac{\beta}{r},\tag{3}$$

with the shear wave velocity at the source, β, and a constant k that relates to the spherical average of the corner frequency for a specific theoretical source model. By combining Equations 2 and 3 the sometimes called "Brune type" stress drop can be computed

$$\Delta\sigma = \frac{7}{16}\left(\frac{f_c}{k\beta}\right)^3 M_0.\tag{4}$$

We described above the procedure to obtain the value for the spherically averaged corner frequency f_c (Equation 1). To compute the stress drop, we rely on additional information for the other parameters.

Münchmeyer et al. (2020) provide a refined and consistent magnitude catalog for the data set of Sippl et al. (2018). We derive the seismic moment from their corrected local magnitude catalog by presuming sufficient similarity to moment magnitude and then using the standard relation ($M_W = 2/3(log_{10}(M_0) - 9.1)$).

Because of the large spatial extent of our event distribution, shear wave velocities vary considerably, and we use the extrapolated two-dimensional velocity model from Bloch et al. (2014) to determine the shear wave velocity individually for each event pair. For the k parameter we take the standard value from Madariaga (1976): $k_p = 0.32$ for P phases. Following Prieto et al. (2004) and Abercrombie et al. (2016), we estimate the relation of P to S phase derived corner frequencies for our entire data set, as shown in Figure 2.
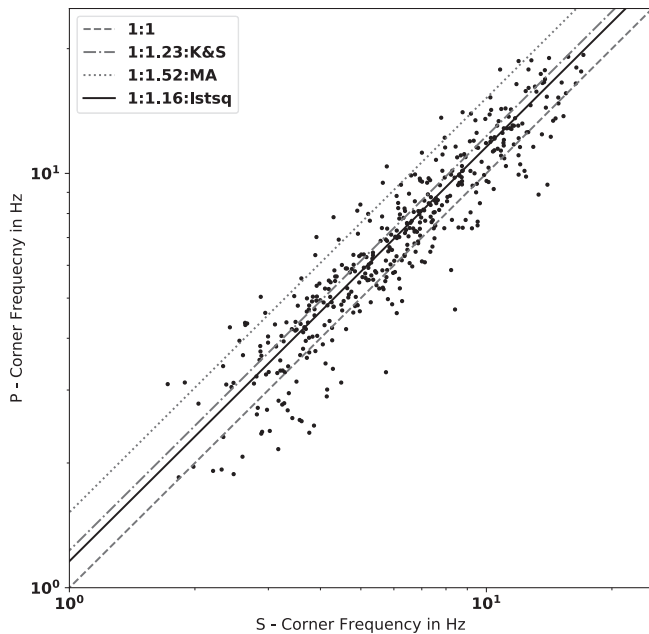
Figure 2. *P* phase based versus *S* phase based corner frequencies. The four different lines are the 1:1 line, the 1:1.23 line illustrative for one of the rupture models of Kaneko and Shearer (2014) where $v_r/\beta = 0.7$, 1:1.52 the value obtained by Madariaga (1976) for $v_r/\beta = 0.9$, and our estimate 1:1.16 obtained by fitting a least square regression line to the data. Using an empirical k_p/k_s ratio allows to combine *P* and *S* phase based stress drop estimates.

The procedure provides a best fitting ratio of $f_{c_p} / f_{c_s} = k_p / k_s = 1.16$ yielding a value of $k_s = 0.28$ for *S* phases. By choosing both k values accordingly, we obtain comparability of the resulting stress drop values from *P* to *S* phases.

When the complete data set is processed we find that many target events have not only one P and S phase based stress drop estimate (which was obtained by taking the median over all recording stations), but they may also have additional EGF events. In these cases, we collect the results and take the median of all estimates to enhance stability further. We also make use of the redundancy information from these event families to estimate the robustness of our approach as described in the uncertainty section.

3.4. Data Example

We illustrate our realization of the spectral ratio approach for one event pair in Figures 3 and 4. Figure 3 shows all pre-processed velocity traces available for both events. The selected (here P) phase windows are highlighted in gray. Figure 4 displays the corresponding spectra, their spectral ratios with the obtained fit curves for the Boatwright spectral model and the station wise variation of corner frequency with the overall median for the target event. The stress drop value of $\Delta\sigma = 1.7$ MPa is then computed from the average spectral ratio (Figure 5). Note the good consistency between the individual measurements, their median f_c and the result computed from the average ratio. Additional figures are given in the supplement, including examples based on S phase spectra, using the Brune model for fitting the corner frequency and from events with different magnitudes (Figures S3–S17).

3.5. Limitations & Uncertainties

In this section, we will discuss data limitations of this study. Thereafter, we will discuss sources of uncertainty inherent to the stress drop estimation procedure and compute an approximate error for the stress drop computation.

3.5.1. Limitations

The estimation of spectra-derived properties is always limited by the bandwidth that can be reliably resolved. In this study, we use recorded 100 Hz velocity data which was bandpass filtered from 0.8 to 40 Hz. To allow a sufficiently high number of frequency points above the corner frequency in order to fit the spectral model to the data, results for f_c were limited between 1 and 20 Hz. This limitation, however, constitutes a selection bias on possible corner frequencies. As a consequence, high stress drop events or low stress drop events may be suppressed systematically. We find evidence for such an effect when studying the scaling relation between moment and corner frequency in the Results & Discussion section.

Due to their long recording period and consistency of data availability, we restrict our analysis to the 23 IPOC stations, which are also the base for the seismicity catalog of Sippl et al. (2018). On average 17 traces contribute to a single stress drop measurement. Having verified that no major variation of statistical properties occurs, we accept results down to four contributing traces. Some stress drop values, therefore, are estimated using only relatively few stations.

As a consequence of the event locations and station positions, the station layout for most events is one-sided and we cannot rule out an impact of possible rupture directivity on the corner frequency. Also, the event depths and their source plane orientations may impact the stress drop estimates as f_c varies depending on the takeoff angle (Kaneko & Shearer, 2014). Since most events are located close to the plate interface, we
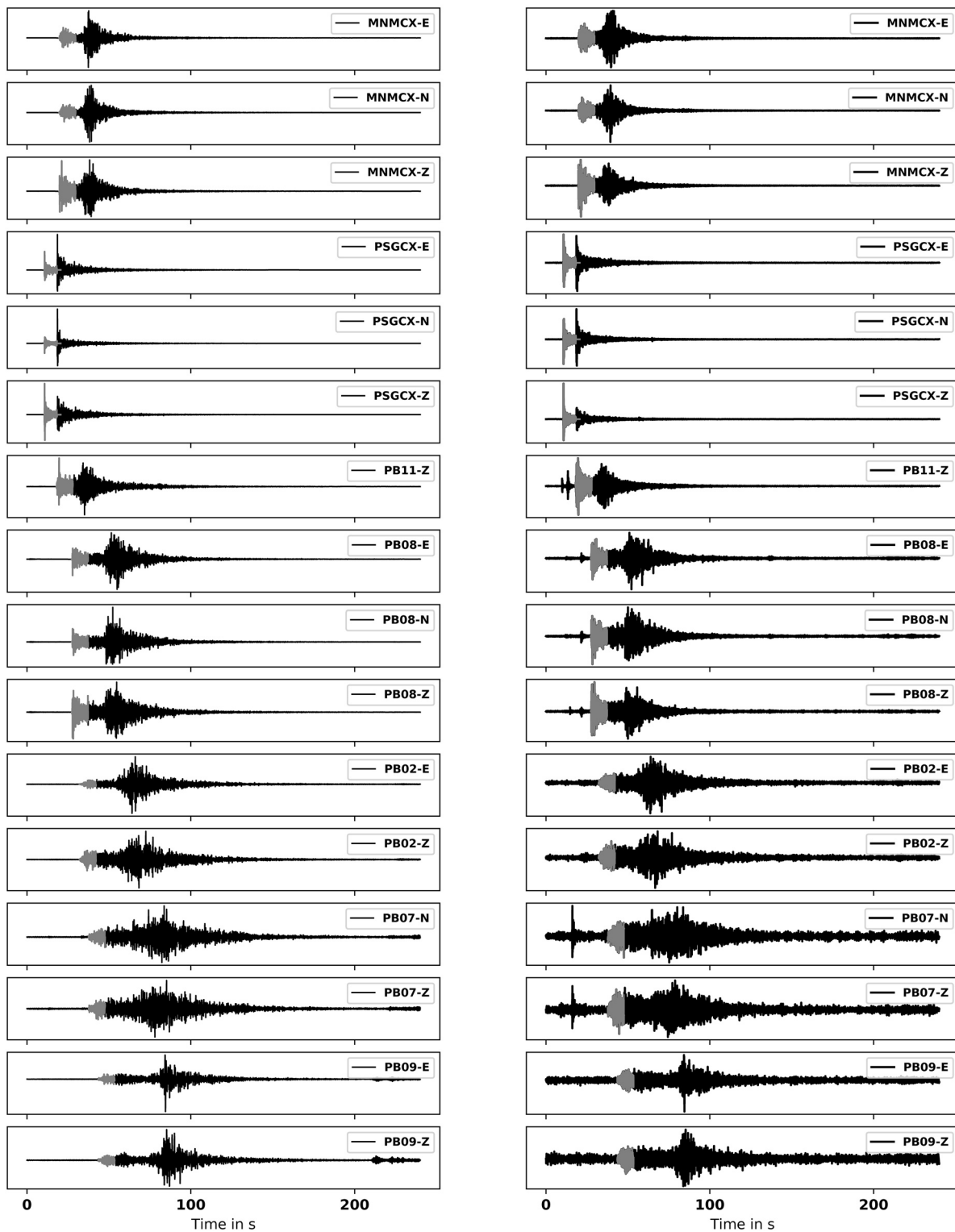
Figure 3. Velocity traces with highlighted *P* phase windows for an exemplary event pair. (Left) Pre-processed velocity traces of the target event, (right) pre-processed velocity traces of the smaller magnitude EGF event. Only the traces which comply with our selection criteria are displayed. The labels contain station and component names. The P picks are taken from the catalog for the target event and they were transferred to the EGF event based on the inter event time. The header specifies event origin times and magnitude of the target event. EGF, empirical Green's function.
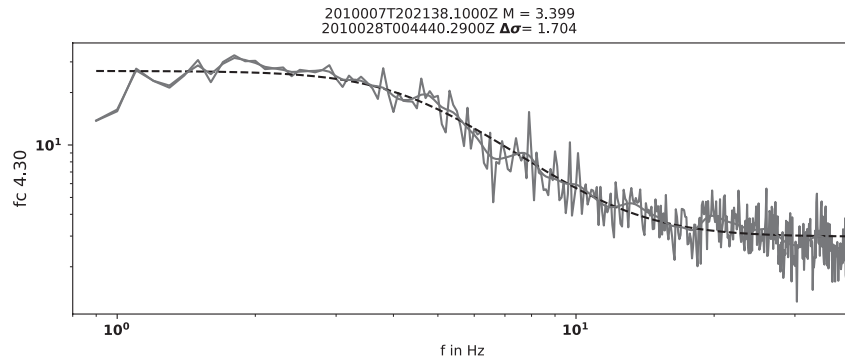
2010007T202138.1000Z M = 3.399
2010028T004440.2900Z
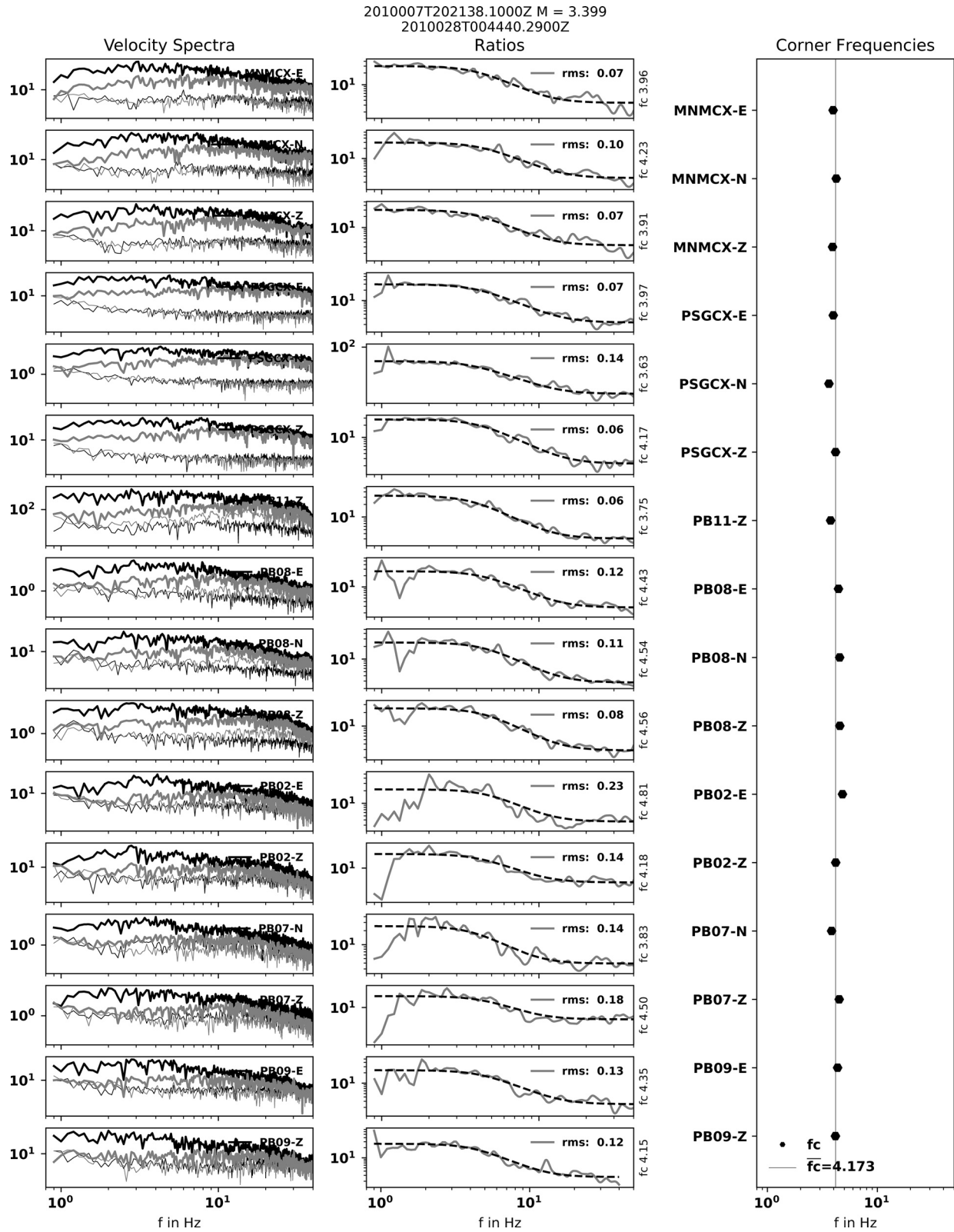
Figure 5. Average spectral ratio computed from the median for each frequency point over all traces shown in Figure 4. The curve is smoothed (Konno & Ohmachi, 1998) and then fitted with the Boatwright spectral model ($n = 2$) to obtain the corner frequency, $f_c = 4.30$ Hz, of the target event which is used to compute the stress drop, $\Delta\sigma = 1.7$ MPa.

make a first order assumption of similar rupture mechanisms (Cesca et al., 2016) and similar locations relative to the station network. Then, geometric conditions are comparable for all events, and we expect only a minor effect on stress drop variations between events.

Another possible selection bias arises by the choice of suitable empirical Green's function events. Using inappropriate EGF events would result in reduced validity of the deconvolution procedure to recover the spectra of the target events. We apply a high cross-correlation threshold of cc = 0.8 measured over a long time window of 35 s. The threshold has to be exceeded at a minimum of three stations. Additionally, we require a minimum magnitude difference of $\Delta M \geq 1$ between target and EGF event. These are comparably rigorous restrictions and, as reported in Abercrombie (2015) and Abercrombie et al. (2016), we do not observe any influence on the stress drop estimate by varying the cc or ΔM requirements above the applied thresholds. By application of this criteria, we limit the analysis to regions of high event occurrence rates where EGFs may be found. Other areas remain unsampled.

To enhance stability of the computation of the spectral ratio, we smooth each spectrum before fitting (Huang et al., 2016). We use the Konno and Ohmachi (1998) smoothing operator to account for the logarithmic distribution of sample points in each smoothing window. We verified that only a negligible variation of f_c is introduced by the smoothing, using a simple synthetic source spectrum with added Gaussian white noise (please see the electronic supplement and Figure S22 for further explanation).

The choice of the spectral model has a systematic influence on the estimated corner frequency. Because of their spectral shapes, the Brune model provides a lower f_c than the Boatwright model. We tested both models and found that the Boatwright model overall describes our data better (see Figures S5 and S6 ff. in the supporting information). We therefore, selected it for the analysis. By optimizing additionally for the falloff rate n in Equation 1, it is in principle possible to further improve the fitting and decrease the standard deviation of the parameter f_c while introducing another uncertainty for n itself (Trugman & Shearer, 2017). We refrain from this approach and fix $n = 2$ which makes the results somewhat more comparable (Kaneko & Shearer, 2014).

3.5.2. Uncertainties

Keeping in mind the upper mentioned limitations and possible sources of systematic bias, one can analyze the statistical error of stress drop within the data set by an assessment of the uncertainty of the contributing factors in the Brune type stress drop formula.

Figure 4. Velocity spectra of the example events from Figure 3 (left). Black is the target event, gray the EGF event. The thinner lines are the corresponding noise spectra. The smoothed spectral ratio is computed for each trace and the Boatwright spectral model is fitted to the data (center). Corner frequency (f_c) and RMS values are given for each spectrum. The corner frequencies are then plotted trace wise where stations are sorted from north to south (right) such that azimuthal variability and outliers could be observed. The median value, $\overline{f_c}$, is indicated by the vertical line. The header states event origin times and magnitude of the target event. EGF, empirical Green's function.
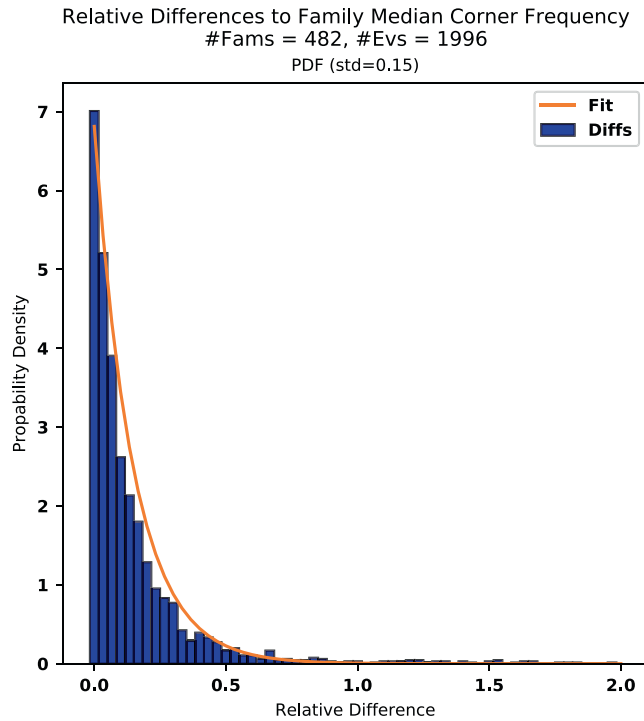
Figure 6. Histogram of relative differences to the family specific median corner frequencies (For each of the 482 target event families one single median f_c is calculated and the individual difference of each f_c estimate (in total 1996) to this median is divided by this median). The distribution is normalized and a PDF with exponential shape is fitted to the data. Note that the great majority of event families show very similar stress drop estimates (difference is smaller 0.5) which means that different phases and different EGFs produce similar corner frequency estimates for a given target event. EGF, empirical Green's function.

To evaluate the statistical error of the corner frequency of our analysis we exploit the redundancy of f_c measurements within our data set. Because P and S phase based corner frequencies are computed separately, most events have at least two independent f_c estimates. Many events also belong to so called event families for which the target event has two or more associated EGF events. We compute the median corner frequency for each target event from all P and S phase based measurements within an event family and calculate the difference of each single estimate to this median value divided by the median value. We refer to this value as the relative difference. Figure 6 shows the distribution of relative differences combined for 482 event families. Counting P and S phase, separately, a total of 1996 EGF events were used. The histogram is scaled to fit a PDF to the data. The best fitting PDF has exponential shape (PDF = $\lambda e^{-\lambda x}$). We compute the corresponding standard deviation std = $1/\lambda = 0.15$. This value compares well with the range of normalized standard deviations for multiple station estimates provided by Abercrombie (2015) (their Figure 4) who explicitly investigated EGF uncertainty factors. We will use the obtained value as an approximate relative error, that is, $\delta(f_c) = 0.15\%$.

The true rupture velocity is almost always unknown and poses another source of uncertainty. In the frame of Brune type stress drop estimation, it is usually treated in combination with the rupture mechanism and the observation geometry, which is expressed by the k value in Equation 2 (Brune, 1970; Madariaga, 1976; Sato & Hirasawa, 1973). Kaneko and Shearer (2014) show in detail that different combinations of k_s and k_p for S and P phases, respectively, can be assigned to different source models and rupture velocities. In principle, k is also station-specific and depends on the takeoff angle under which the ray leaves the source. Since the event-specific k values are generally unknown, we follow the approach of Prieto et al. (2004) and determine the k ratio empirically. Figure 2 displays the event wise and spherically averaged corner frequencies of P phase versus S phase for the entire data set. The computed regression line gives the ratio for which both phases provide on average the same stress drop for a given event over the entire data set. According to Kaneko and Shearer (2014) our estimate of $k_p/k_s = 1.16$ could represent overall symmetrically rupturing circular sources with a relatively slow rupture velocity of $v_r \approx 0.6\beta$. Figure 2 demonstrates that the uniform k_p/k_s ratio holds well for the majority of events, but it also indicates differing ratios for some events. A possible explanation for this observation are deviations in the rupture characteristics such as rupture mechanism, directivity or deviating fault plane orientation.

Next, knowledge of the seismic moment M_0 is required to compute the stress drops (Equation 2). We derive it from the magnitudes provided by Münchmeyer et al. (2020). Although uncertainties for the magnitudes are very low in their catalog - the authors give standard deviations in the low percentage range (0.5%–2.5%)—this translates to about ten-fold relative errors for the corresponding seismic moment, i.e., the relative error for the moments range between 10% and 30% for most events.

The last parameter in the stress drop equation is the shear wave velocity β. Especially in a subduction zone setting, phase velocity may vary significantly on a 10 km scale. It is consequently important to apply the best velocity model available. We obtain β from a pseudo three-dimensional velocity model created by Bloch et al. (2014) (see Figure S27) and use individual values for each target event depending on its location. Assuming correct event locations, we expect a relative error in the shear wave velocity of about 5%.

Combining the relative errors obtained as explained above ($\delta f_c = 15\%$, $\delta M_0 = 30\%$, $\delta \beta = 5\%$) and conservatively using doubled error values, that is, two times the standard deviation, the relative error from the stress

drop computation is about 200% ($\approx 3(2\delta f_c + 2\delta\ \beta) + 2\delta\ M_0$) according to Equation 4. Note that this is still much smaller than the variability of the stress drop values in our final result catalog, which vary over 2–3 orders of magnitude. We conclude that our workflow is reasonably well suited to produce meaningful results and that it is capable of resolving actual variations of stress drop, while keeping in mind the limitations that affect the whole data set.

4. Results & Discussion

The workflow is applied to the entire data set of 2,610 events (Figure 1). The analysis yields 1,237 P phase based and 1,396 S phase based stress drop estimates. These numbers reduce when accounting for the fact that a target event may have multiple EGF events. As explained earlier we combine the P and S phase derived stress drops by fixing the ratio of the k parameters to the previously calibrated value $k_p/k_s = 1.16$ (Figure 2). For each target event, we then merge the measurements from P and S phases and from additional EGF events, if present, by taking the median over all single estimates. This procedure yields stress drop estimates for 534 target events. Their distribution is plotted event wise in Figure 7. The resulting stress drops show a well pronounced log-normal distribution with an overall median stress drop of $\Delta\sigma = 4.36$ MPa displayed in Figure 8. This value is of the same order as the independently estimated stress drops for the Iquique earthquake, $\Delta\sigma = 7.66$ MPa, and its biggest aftershock, $\Delta\sigma = 4.28$ MPa by Ye et al. (2016), derived with a time domain approach.

The stress drop map reveals a heterogeneous distribution. Note that the spectral ratio approach is limited to those subregions where suitable EGF events exist. Event density is much higher on the part of the interface that lies updip of the maximum slip patch of the 2014 Iquique event. This observation reflects the overall very high updip seismic activity related to the megathrust event.

We attempt to identify regions of characteristic stress drop behavior by dividing the study region into grid cells and computing the median stress drops for each cell, similar to the approach by Uchide et al. (2014). The results are shown in Figure 8. No smoothing is applied between cells. Average values dominate and in principle, stress drop appears to be distributed very heterogeneously throughout the map. We noted an interesting patch of elevated values north of the nucleation point of the $M_w 8.1$ mainshock, as well as a larger patch of increased values west of the hypocenter of the $M_w 7.6$ aftershock, both highlighted by black outlines. When interpreted as stress barriers marked by higher roughness, they could possibly indicate domains of the interface which inhibited further growth of the rupture area of the large Iquique event, as suggested for example, for the 2011, Tohoku-Oki earthquake by Uchide et al. (2014). The predominant rupture directivity of both events, the main event rupturing toward south east and the aftershock toward east (Folesky, Kummerow, Asch, et al., 2018) could then be interpreted as a consequence of such an existing barrier.

To analyze the spatial dependency further we plot spatial sections in Figure 9. In addition to the estimated stress drops, the median values for bins of 0.1° widths are overlain for better visualization. Again, no smoothing is applied between bins.

In the west-east section, bin values are continuously close to the overall average, with a slight tendency of increase toward east and few elevated values to the east.

The north-south section also shows mainly close to average values except for a few domains of increase, for example, at 19.5°S and 20.5°S. These correspond to the higher stress drop value patches observed previously and highlighted in the map view. South of 20.5°S, Sippl et al. (2018) identified increased upper plate seismic activity, which was suggested to correlate with a reduced interplate locking (Li et al., 2015; Moreno et al., 2016). We observe here a bin comprising predominantly small stress drop vales. If this behavior extends further toward the south (neglecting the last bin with only few high stress drop events, which are also located further east), this could corroborate their observation when confirmed with more data.

The depth view reveals fairly stable results of median stress drop for different depths. Abercrombie et al. (2016) report similar observations of non-significant stress drop variation with depth for earthquake sequences in shallow depth ranges (5–35 km). Below, stress drop values are slightly elevated for several
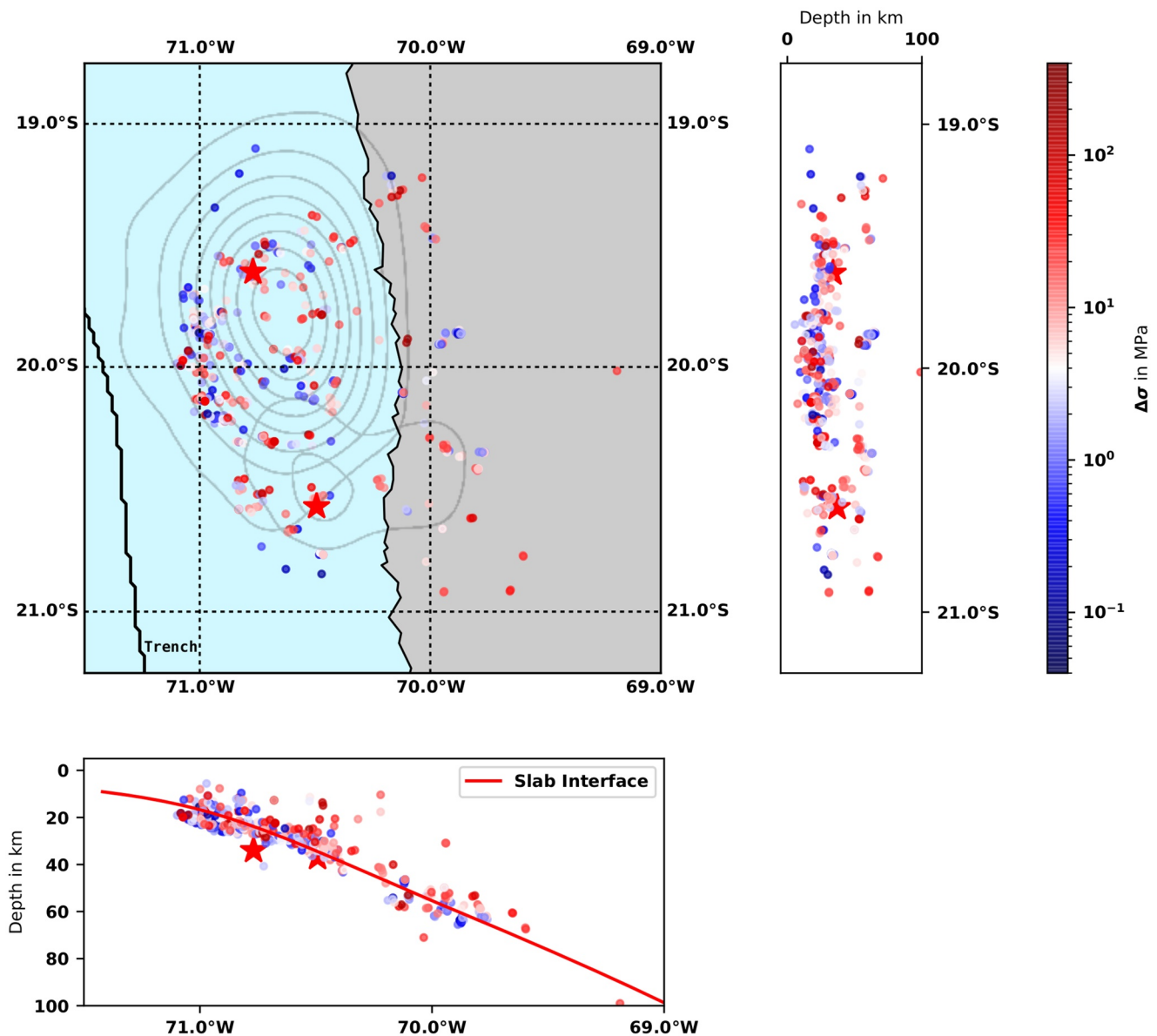
Figure 7. Stress drop distribution for 534 target events in map and depth views. Color indicates the stress drop value. The red stars indicate the hypocenters of the M_W8.1 Iquique event and the M_W7.6 largest aftershock. Underlain is the coseismic slip distribution in 0.5 m increments taken from Schurr et al. (2014). The red line in the west-east depth section delineates the slab interface from Hayes et al. (2012).

kilometers till about 55 km depth and then decrease again. Interestingly, this curve shape is relatively similar to the global observation by Allmann and Shearer (2009) who report a slight rise of values starting at 35 km and falloff at about 55 km depth.

The observation of a stable median stress drop down to 70 km is in contrast to findings from the Japanese subduction zone (Uchide et al., 2014), where a strong depth dependence was observed. For northern Chile, Derode and Campos (2019) report evidence for depth dependence of stress drop from 96 events of two different clusters. In their study, however, the velocity spectra are directly fitted with Brune's model, and path effects are not corrected for. We do not observe their reported clear depth dependence of stress drops in our extended data set.

The remaining section in Figure 9 shows the stress drop as a function of event distance from the slab interface. We use the reference model of Hayes et al. (2012) to compute this distance. A roughly symmetrical
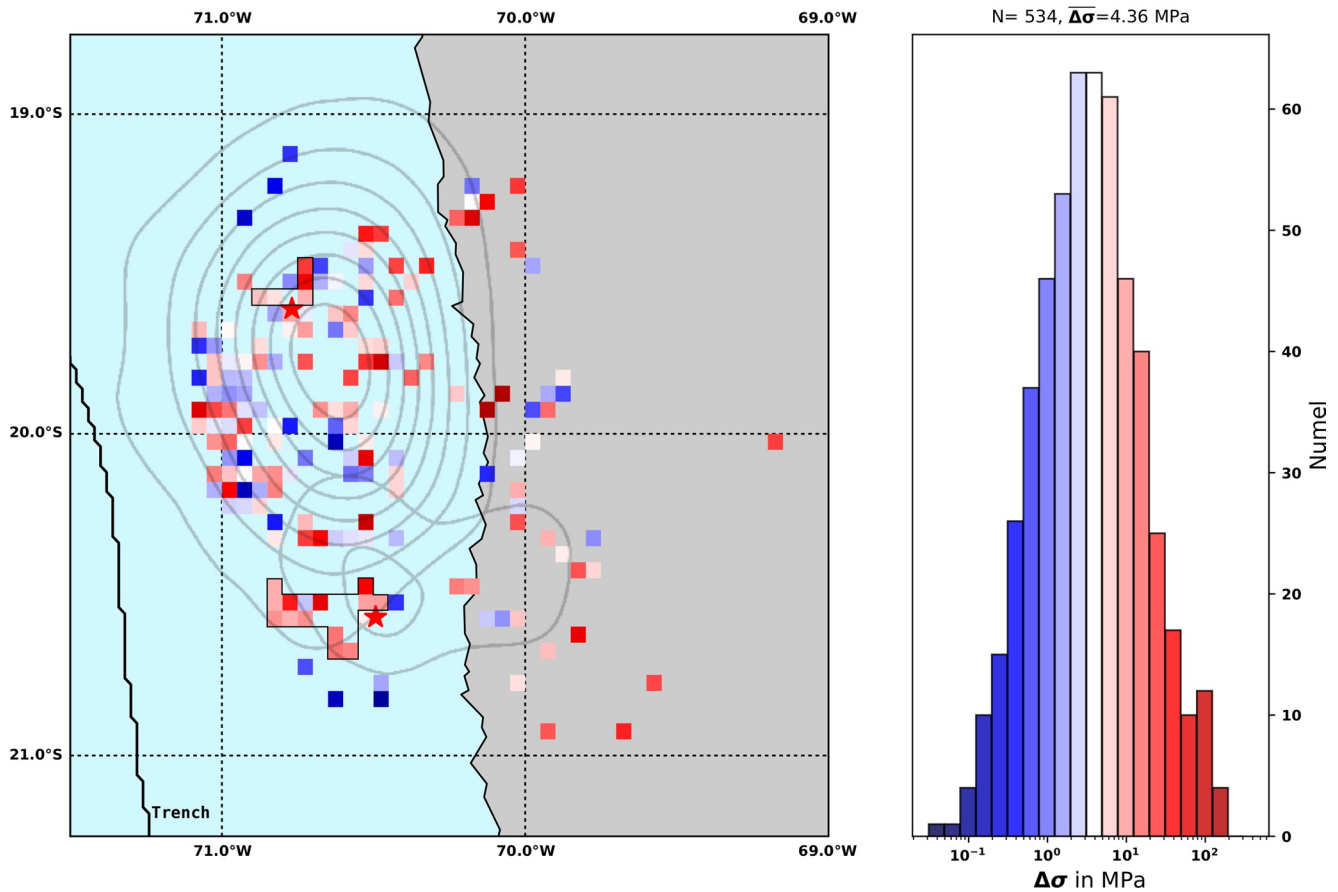
Figure 8. Stress drop distribution averaged on a regular horizontal grid. In each grid cell the median for all occurring events is computed and displayed in color according to the color scheme of the histogram. The red stars indicate the hypocenters of the $M_W 8.1$ Iquique event and the $M_W 7.6$ largest aftershock for orientation. Underlain are the corresponding coseismic slip distributions in 0.5 m increments taken from Schurr et al. (2014). Two regions of increased stress drop are highlighted by a superimposed black contour line (cf. text). The histogram shows the distribution of stress drops for all 534 target events with their median of $\overline{\Delta\sigma} = 4.36$ MPa.

behavior can be noticed. From −7.5 to 7.5 km close to average values are observed, and beyond these distances, the median stress drop is notably elevated. Here, a possible explanation could be the maturity of the rupture surfaces. While close to the interface rupture surfaces have been activated repeatedly, the intraplate seismicity occurs on more intact fracture zones. These less mature faults could then produce higher stress drop events (e.g. Choy & Kirby, 2004; Sagy et al., 2007). Or, in other terms, the friction coefficient increases when receding from the interface into the plates. In combination with the previously noted only weakly pronounced stress drop dependence with absolute depth, this observation suggests that the fault strength and faulting regime play more important roles than the lithostatic stress.

The long recording period of over 10 years of consistent seismological observations of the northern Chilean subduction zone (IPOC, 2006) also provides a rare opportunity to study the temporal evolution of stress drop. We display the temporal sequence of stress drops in Figure 10 for the time period 2009–2017. The data is dominated by the fore- and aftershock seismicity of the 2014 Iquique earthquake. In general, the 13-weeks median stress drop binned values vary (almost randomly) around the overall median. The variation, however, is based only on a limited number of events and should be interpreted with caution. Zooming into the seismically highly active weeks around the Iquique event shows that average values are measured during the 2 weeks following the large, $M_w 6.6$ foreshock. A positive jump of stress drop from 4.0 to about 8 MPa is observed just after the mainshock (ignoring the high stress drop bin before), followed by a steady decrease of stress drop median values down to about 1 MPa over a time interval of 2–3 weeks. Then, the trend reverses and the median stress drop rises again to about the average value.
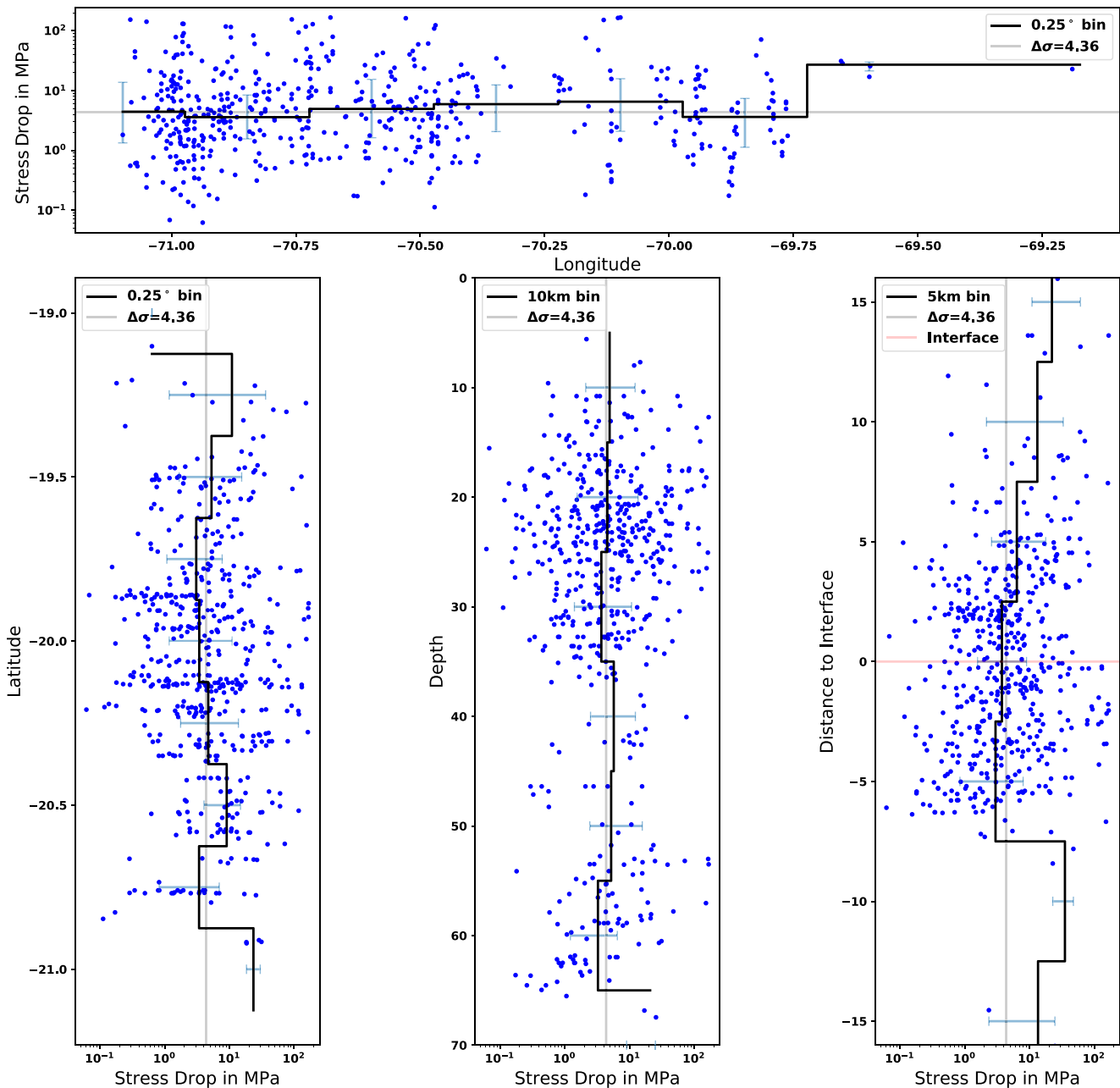
Figure 9. Stress drop variation in the spatial domain. The top panel shows stress drop estimates versus longitude. Below, the stress drop distribution is shown from north to south, against depth and relative to the plate interface from left to right, respectively. The binning interval is given in the plot legends. No smoothing is applied. The solid line traces the median value computed for each bin separately. To indicate the spread of values in each bin we plot a blue error bar from the median of the upper to the median of the lower half of values, which are separated by the overall median in the bin. In all plots the median of the entire data set ($\overline{\Delta\sigma} = 4.36$ MPa) is underlain as a gray line. In the last panel positive distance values refer to events located above the plate interface (red line), negative values to events below it.

The average stress drop in the same time window, that is, the median over 2 weeks before compared to the median of 4 weeks after the main event changes from 3.98 to 4.48 MPa while the overall median stress drop from before to after the Iquique event decreases from 4.55 to 4.31 MPa.

Such an observation appears inconsistent until the influence of the spatio-temporal aspect in the data is considered. To illustrate this, we produced additional maps for events that occurred before the main earthquake, after the main event and maps comprising only direct foreshocks or aftershocks. Please see
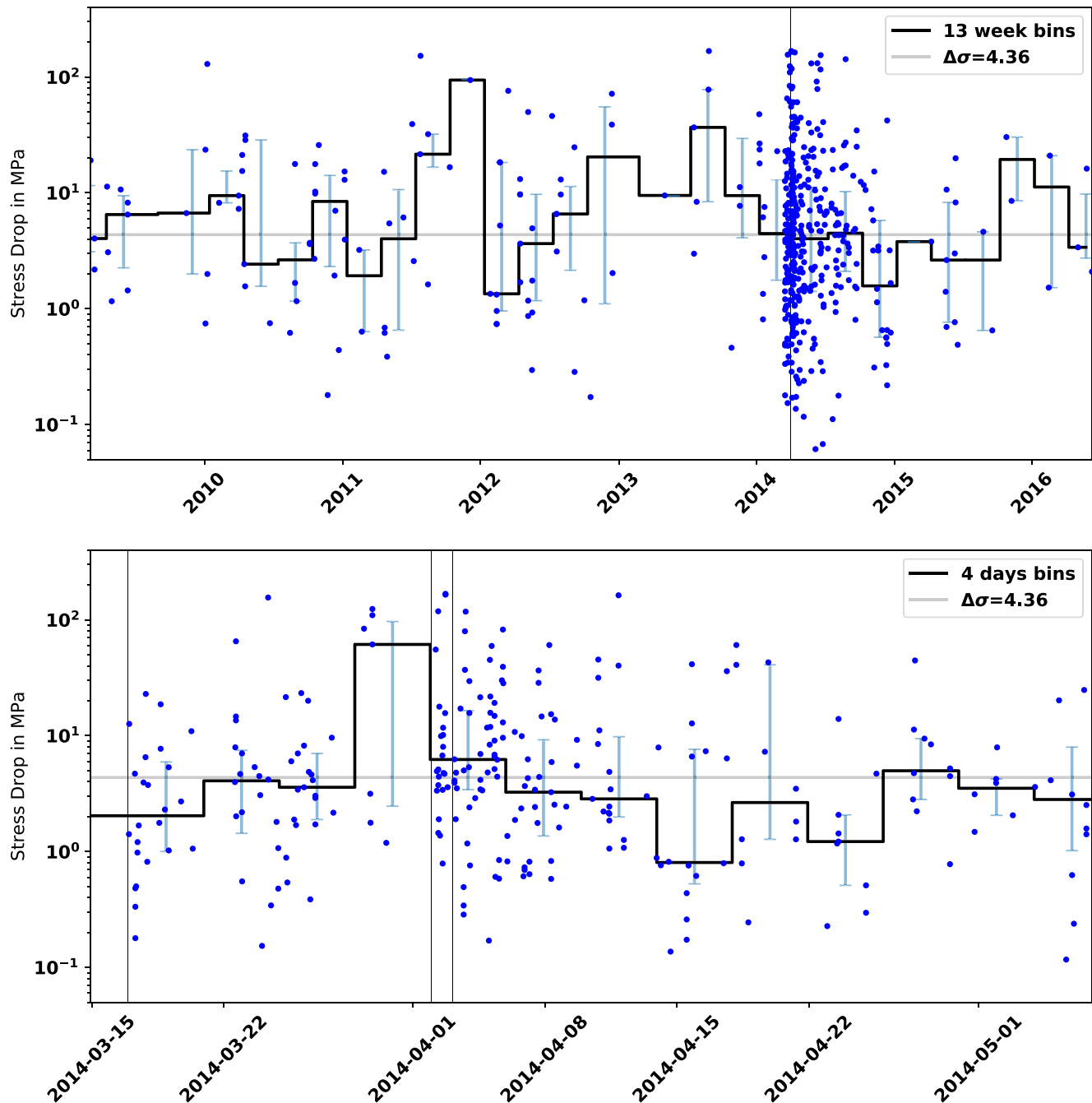
Figure 10. Stress drop variation in the time domain. The top panel shows stress drop values for the period from beginning of 2009 to end of 2016. The solid black line traces the median values for bins of 13 weeks time span each. The gray bar indicates the period displayed in the bottom panel. It shows an 6 weeks time period of strong seismic activity around the Iquique mainshock starting about 2 weeks before the event. The three vertical gray lines denote the origin times of the M_W6.6 foreshock, the M_W8.1 mainshock, and the M_W7.6 aftershock. Bin width is 4 days; no smoothing is applied. To indicate the spread of values in each bin we plot a blue error bar from the median of the upper to the median of the lower half of values, which are separated by the overall median in the bin. In all plots the median of the entire data set ($\overline{\Delta\sigma}$ = 4.36 MPa) is underlain as a gray line.

Figures S18–S21 in the supporting information. The maps indicate that the variability of the median stress drop value is likely to arise from variable event occurrence locations in the split data sets. Unfortunately, a differential comparison between fore and after main event maps failed due to the limited overlap between event locations. Still, this demonstrates that spatial and temporal stress drop variability has to be interpreted with caution.
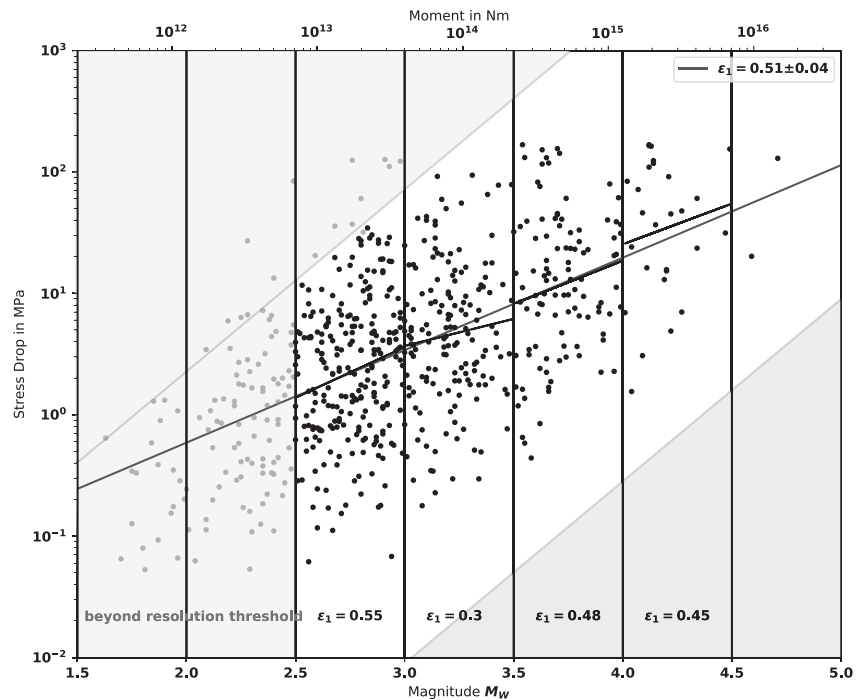
Figure 11. Scaling of stress drop with seismic moment. We fit the data with a standard least square regression where $log_{10}(\Delta\sigma) = \varepsilon_0 + \varepsilon_1 log_{10}(M_0)$. The legend gives the result for ε_1 and its standard deviation. At the bottom ε_1 values for the individual bins are displayed. Gray areas are beyond the resolution capacity of this study. Boundaries are defined by the 20 Hz and the 1 Hz lines and $M = 2.5$. A clear dependence of stress drop on seismic moment is observed not only for the entire data but also for each individual bin.

We notice that the variation of stress drop in time is not independent of the target event magnitudes that were used to compute the stress drop estimates. In fact, the variation of magnitude is similar to the variation of stress drop (Figure S23). This indicates a correlation between moment and stress drop.

The dependency between stress drop and seismic moment was analyzed in many stress drop studies, with diverging results. Shearer et al. (2006) and Abercrombie (1995) reported moment independent stress drops, whereas several recent studies (in parts of the same groups of researchers) observed a relation between stress drop and seismic moment (Abercrombie, 2014; Abercrombie et al., 2016; Trugman, 2020; Trugman & Shearer, 2017). Also, regional differences of this correlation have been reported lately (Trugman & Shearer, 2017). For the northern Chilean subduction zone interface seismicity, we observe a clear increase of stress drop with moment (Figure 11). Fitting a standard least square regression line where $log_{10}(\Delta\sigma) = \varepsilon_0 + \varepsilon_1 log_{10}(M_0)$ to the data yields a slope of $\varepsilon_1 = 0.51$ (cf. Figure 11). Note that the limited bandwidth has a significant impact on event selection which becomes apparent here. It could contribute to the very strong scaling effect observed. In Figure 11, we additionally provide the binned slope values. Here, the bin that should be affected most by the 20 Hz cutoff shows the highest scaling value and the bin which is best resolved ($3 < M < 3.5$) has the lowest ε_1 value. We additionally test the influence of an increased SNR threshold onto the scaling and, similar to the study by Chen and Abercrombie (2020), we find the ε_1 value to be lower when selection criteria are more restrictive (e.g., $\varepsilon_1 = 0.42$ if SNR = 12). Hence, the reported scaling value is only a best estimate and has to be taken with care, as it is sensitive to the parameters applied in the processing. Nevertheless, we find a strong stress drop scaling with moment in our data. Such an observation does not support the self-similarity assumption of rupture processes for earthquakes. When compared to other stress drop studies our estimates fall into the typical range between 0.1 and 100 MPa (Figure 12). However, we observe a smaller decrease of corner frequency with seismic moment than expected for moment independent stress drops. Cocco et al. (2016) gather data from several studies and conclude that while some works show moment dependent stress drops for their particular, limited magnitude ranges the overall picture still shows a self-similar rupture behavior with
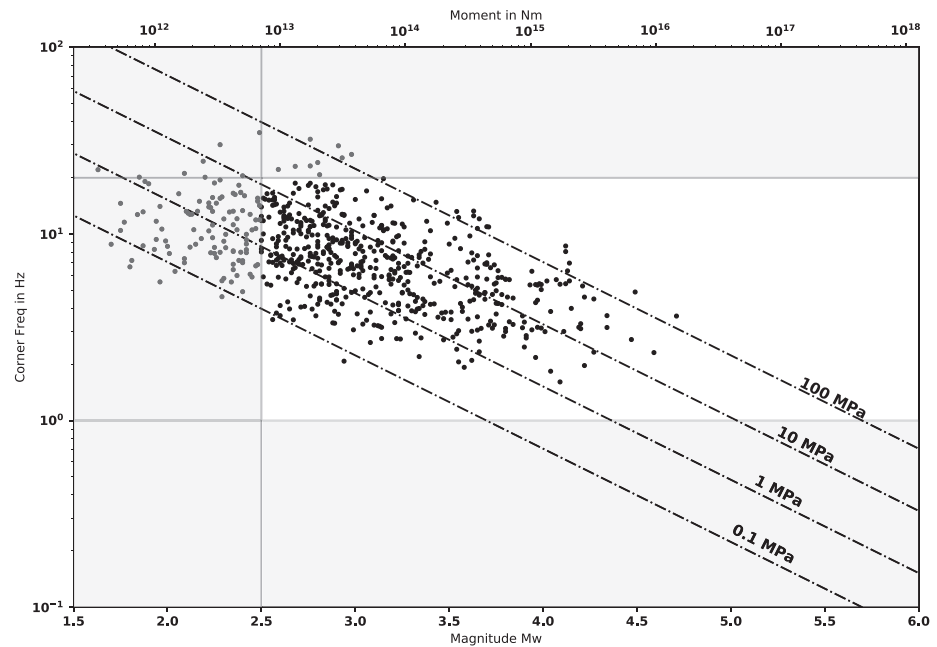
Figure 12. Scaling of corner frequency with seismic moment. The dotted lines indicate constant stress drop levels. The great majority of values lie between 0.1 and 100 MPa with a median of $\overline{\Delta\sigma} = 4.36$ MPa. Note that the decrease of corner frequency with magnitude is less than the rate calculated for a moment independence of the stress drops. Gray areas are beyond the resolution limit of this study (See section Limitations).

no prevailing dependency of stress drop on moment. Note further that the observation of non-self-similarity is made under the assumption of a fixed value $n = 2$. Trugman and Shearer (2017) point out that for their data self-similarity can be obtained by using varied assumptions, for example, by fitting the spectral model with a different falloff rate.

The observed dependence of stress drop on seismic moment raises the question to what extent the observations of stress drop variability made in this work are due to magnitude variation. To assess this issue we test the spatial and temporal variability under the assumption of a moment-independent stress drop. For this, we correct the resulting stress drop values for the gradient computed in Figure 11 such that the gradient vanishes and the median stress drop is preserved (see Figure S24). We then recompute Figures 9 and 10. The resulting Figures S25 and S26 show that the earlier observations of spatio-temporal stress drop variability are generally persistent although the range of variability decreases. The initially observed stress drop variation, therefore, is a combination of both effects, a change in stress drop and a change in earthquake moments.

The procedure described in this article is designed for large data sets where limited knowledge on the events is presumed. As demonstrated by Kaneko and Shearer (2014, 2015) rupture processes may be far more complex than we can assess with current seismological networks. Consequently, it is important to acknowledge the limitations of a given data set. In the case of the IPOC observation system, we deal with a one-sided observation geometry for most events of this study, and we can only presume that averaging over as many stations as possible provides a reasonable estimate of the corner frequency for a given event. This may be sufficient to extract the more general features of the data set which is the main objective of the present study. When conclusions are drawn from particular observations of a small number of events, special caution should be taken.

Theoretically, it is possible, albeit out of the scope of this work, to enhance the precision of single event stress drop estimates. For this, the event rupture plane must be known, at best complemented by information on the rupture behavior such as the rupture velocity and directivity. For our study area information on fault planes exists (e.g. Cesca et al., 2016; Bloch, Schurr, et al., 2018) and it has been demonstrated that

a significant amount of events show rupture directivity (Folesky, Kummerow, Asch, et al., 2018; Folesky, Kummerow, & Shapiro, 2018). The inclusion of such information into our workflow is in principal possible, and it could help in the future to further improve the stress drop estimates.

5. Conclusions

We compute stress drop estimates for 534 earthquakes in the subduction zone of northern Chile. The events occurred at or close to the plate interface in the rupture region of the 2014 M_w8.1 Iquique event. The computed stress drops are log-normal distributed and range mostly from 0.1 to 100 MPa with a median value of 4.36 MPa. The spatial distribution is heterogeneous but shows no clear dependence on depth, longitude or latitude. We find, however, a slight increase of median stress drop with distance to the plate interface. We also identify a few small patches of increased stress drop. We additionally observe a temporal variation of the median stress drop associated with the Iquique megathrust event. Just after the event, average stress drop increases, followed by a steady decrease lasting for several weeks until the trend reverses and the median stress drop value recovers to the long term average. Furthermore, we find indications that stress drop depends on the seismo-tectonic regime (cf. classification in Sippl et al., 2018).

The stress drop estimates show a clear scaling with seismic moment. We find the empirical relation $log_{10}(\Delta\sigma) = \varepsilon_0 + 0.51\ log_{10}(M_0)$ by fitting a regression line to the data. We show that this relatively strong dependency on moment is impacted by data limitations (frequency range) and decreases when selecting only very high quality data (high SNR). Still, this data set suggests a break of self-similar rupture scaling under the given assumptions.

It is planned to extend the work to the complete data set provided by Sippl et al. (2018) in the near future. Then, not only stress drop estimates for more than the tenfold number of earthquakes will be available, but also events from multiple distinct seismically active regions of the northern Chilean subduction zone will be processed consistently for the first time, potentially allowing for a broader comparative study.

Data Availability Statement

Seismograms used in this study were recorded by the seismic CX-net of the Integrated Plate boundary Observatory Chile (IPOC, 2006) using STS-2 broadband seismometers. Data were obtained from the EIDA/ GEOPHONE web page (eida.gfz-potsdam.de/webdc3/or geofon.gfz-potsdam.de/waveform/, accessed on 2017/09/24, https://doi.org/10.14470/PK615318). Picks, magnitudes, and event hypocenter were taken from Sippl et al. (2018). Data processing and figure production were mainly performed using Python3.5.1 (python.org) and packages IPython4.2.0 (Pérez & Granger, 2007), NumPy (Walt et al., 2011), Matplotlib (Hunter, 2007), ObsPy (Beyreuther et al., 2010) and SciPy (Virtanen et al., 2020). Some figures were refined using Inkscape (inkscape.org). Results from this study are summarized in a table described and made available in the electronic supplement.

References

Abercrombie, R. E. (1995). Earthquake source scaling relationships from −1 to 5 ML using seismograms recorded at 2.5-km depth. *Journal of Geophysical Research*, *100*(B12), 24015–24036. https://doi.org/10.1029/95jb02397

Abercrombie, R. E. (2014). Stress drops of repeating earthquakes on the San Andreas fault at Parkfield. *Geophysical Research Letters*, *41*(24), 8784–8791. https://doi.org/10.1002/2014gl062079

Abercrombie, R. E. (2015). Investigating uncertainties in empirical Green's function analysis of earthquake source parameters. *Journal of Geophysical: Res. Solid Earth*, *120*(6), 4263–4277. https://doi.org/10.1002/2015jb011984

Abercrombie, R. E., Bannister, S., Ristau, J., & Doser, D. (2016). Variability of earthquake stress drop in a subduction setting, the Hikurangi Margin, New Zealand. *Geophysical Journal International*, *208*, 306–320.

Abercrombie, R. E., Poli, P., & Bannister, S. (2017). Earthquake directivity, orientation, and stress drop within the subducting plate at the Hikurangi margin, New Zealand. *Journal of Geophysical Research: Solid Earth*, *122*(12), 10–176. https://doi.org/10.1002/2017jb014935

Allmann, B. P., & Shearer, P. M. (2009). Global variations of stress drop for moderate to large earthquakes. *Journal of Geophysical Research: Solid Earth*, *114*(B1). https://doi.org/10.1029/2008jb005821

Bergman, G. P., Wald, D. J., & Johnson, R. L. (2012). Slab1. 0: A three-dimensional model of global subduction zone geometries. *Journal of Geophysical Research: Solid Earth*, *117*(B1). https://doi.org/10.1029/2011jb008524

Beyreuther, M., Barsch, R., Krischer, L., Megies, T., Behr, Y., & Wassermann, J. (2010). ObsPy: A Python toolbox for seismology. *Seismological Research Letters*, *81*(3), 530–533. https://doi.org/10.1785/gssrl.81.3.530

Bianchi, M., Evans, P. L., Heinloo, A., & Quinteros, J. (2015). *Webdc3 web interface*. GFZ Data Services. https://doi.org/10.5880/GFZ.2.4/2016.001

Bloch, W., John, T., Kummerow, J., Salazar, P., Krüger, O. S., & Shapiro, S. A. (2018). Watching dehydration: Seismic indication for transient fluid pathways in the oceanic mantle of the subducting Nazca slab. *Geochemistry, Geophysics, Geosystems*, *19*(9), 3189–3207. https://doi.org/10.1029/2018gc007703

Bloch, W., Kummerow, J., Salazar, P., Wigger, P., & Shapiro, S. A. (2014). High-resolution image of the North Chilean subduction zone: Seismicity, reflectivity and fluids. *Geophysical Journal International*, *197*(3), 1744–1749. https://doi.org/10.1093/gji/ggu084

Bloch, W., Schurr, B., Kummerow, J., Salazar, P., & Shapiro, S. A. (2018). From slab coupling to slab pull: Stress segmentation in the subducting Nazca plate. *Geophysical Research Letters*, *45*(11), 5407–5416. https://doi.org/10.1029/2018gl078793

Boatwright, J. (1980). A spectral theory for circular seismic sources; Simple estimates of source dimension, dynamic stress drop, and radiated seismic energy. *Bulletin of the Seismological Society of America*, *70*(1), 1–27.

Boyd, O. S., McNamara, D. E., Hartzell, S., & Choy, G. (2017). Influence of lithostatic stress on earthquake stress drops in North America. *Bulletin of the Seismological Society of America*, *107*(2), 856–868. https://doi.org/10.1785/0120160219

Brune, J. N. (1970). Tectonic stress and the spectra of seismic shear waves from earthquakes. *Journal of Geophysical Research*, *75*(26), 4997. https://doi.org/10.1029/JB075i026p04997

Cesca, S., Grigoli, F., Heimann, S., Dahm, T., Kriegerowski, M., Sobiesiak, M., et al. (2016). TheMw8.1 2014 Iquique, Chile, seismic sequence: A tale of foreshocks and aftershocks. *Geophysical Journal International*, *204*(3), 1766–1780. https://doi.org/10.1093/gji/ggv544

Choy, G. L., & Kirby, S. H. (2004). Apparent stress, fault maturity and seismic hazard for normal-fault earthquakes at subduction zones. *Geophysical Journal International*, *159*(3), 991–1012. https://doi.org/10.1111/j.1365-246x.2004.02449.x

Cocco, M., Tinti, E., & Cirella, A. (2016). On the scale dependence of earthquake stress drop. *Journal of Seismology*, *20*(4), 1151–1170. https://doi.org/10.1007/s10950-016-9594-4

Derode, B., & Campos, J. (2019). Energy budget of intermediate-depth earthquakes in northern Chile: Comparison with shallow earthquakes and implications of rupture velocity models used. *Geophysical Research Letters*, *46*(5), 2484–2493. https://doi.org/10.1029/2018gl080962

Eshelby, J. D. (1957). The determination of the elastic field of an ellipsoidal inclusion, and related problems. *Proceedings of the Royal Society of London A: Mathematical, Physical and Engineering Sciences*, *241*, 376–396.

Folesky, J., Kummerow, J., Asch, G., Schurr, B., Sippl, C., Tilmann, F., & Shapiro, S. A. (2018). Estimating rupture directions from local earthquake data using the IPOC observatory in northern Chile. *Seismological Research Letters*, *89*, 495. https://doi.org/10.1785/0220170202

Folesky, J., Kummerow, J., & Shapiro, S. A. (2018). Patterns of rupture directivity of subduction zone earthquakes in northern Chile. *Journal of Geophysical Research: Solid Earth*, *123*(12), 10–785.

Frankel, A. (1982). The effects of attenuation and site response on the spectra of microearthquakes in the northeastern Caribbean. *Bulletin of the Seismological Society of America*, *72*(4), 1379–1402.

Fuenzalida, A., Schurr, B., Lancieri, M., Sobiesiak, M., & Madariaga, R. (2013). High-resolution relocation and mechanism of aftershocks of the 2007 Tocopilla (Chile) earthquake. *Geophysical Journal International*, *194*(2), 1216–1228. https://doi.org/10.1093/gji/ggt163

Goebel, T. H. W., Hauksson, E., Shearer, P. M., & Ampuero, J. P. (2015). Stress-drop heterogeneity within tectonically complex regions: A case study of San Gorgonio Pass, southern California. *Geophysical Journal International*, *202*(1), 514–528. https://doi.org/10.1093/gji/ggv160

Hainzl, S., Sippl, C., & Schurr, B. (2019). Linear relationship between aftershock productivity and seismic coupling in the northern Chile subduction zone. *Journal of Geophysical Research: Solid Earth*, *124*(8), 8726–8738. https://doi.org/10.1029/2019jb017764

Hardebeck, J. L., & Aron, A. (2009). Earthquake stress drops and inferred fault strength on the Hayward fault, east San Francisco Bay, California. *Bulletin of the Seismological Society of America*, *99*(3), 1801–1814. https://doi.org/10.1785/0120080242

Hayes, G. P., Herman, M. W., Barnhart, W. D., Furlong, K. P., Riquelme, S., Benz, H. M., et al. (2014). Continuing megathrust earthquake potential in Chile after the 2014 Iquique earthquake. *Nature*, *512*(7514), 295. https://doi.org/10.1038/nature13677

Hoffmann, F., Metzger, S., Moreno, M., Deng, Z., Sippl, C., Ortega-Culaciati, F., & Oncken, O. (2018). Characterizing afterslip and ground displacement rate increase following the 2014 Iquique-Pisagua M_w 8.1 earthquake, northern Chile. *Journal of Geophysical Research: Solid Earth*, *123*(5), 4171–4192. https://doi.org/10.1002/2017jb014970

Huang, Y., Beroza, G. C., & Ellsworth, W. L. (2016). Stress drop estimates of potentially induced earthquakes in the Guy-Greenbrier sequence. *Journal of Geophysical Research: Solid Earth*, *121*(9), 6597–6607. https://doi.org/10.1002/2016jb013067

Hunter, J. D. (2007). Matplotlib: A 2D graphics environment. *Computer Science and Engineering*, *9*(3), 90–95. https://doi.org/10.1109/mcse.2007.55

Hutchings, L., & Viegas, G. (2012). *Application of empirical Green's functions in earthquake source, wave propagation and strong ground motion studies*. In Earthquake research and analysis-new frontiers in seismology. InTech.

IPOC. (2006). *IPOC Seismic Network*. Integrated Plate boundary Observatory Chile—IPOC, GFZ German Research Centre for Geosciences; Institut des Sciences de l'Univers-Centre National de la Recherche CNRS-INSU, Seismic Network (Vol. Seismic Network). https://doi.org/10.14470/PK615318

Kanamori, H., & Anderson, D. L. (1975). Theoretical basis of some empirical relations in seismology. *Bulletin of the Seismological Society of America*, *65*, 1073–1095.

Kaneko, Y., & Shearer, P. M. (2014). Seismic source spectra and estimated stress drop derived from cohesive-zone models of circular sub-shear rupture. *Geophysical Journal International*, *197*(2), 1002–1015. https://doi.org/10.1093/gji/ggu030

Kaneko, Y., & Shearer, P. M. (2015). Variability of seismic source spectra, estimated stress drop, and radiated energy, derived from cohesive-zone models of symmetrical and asymmetrical circular and elliptical ruptures. *Journal of Geophysical Research: Solid Earth*, *120*(2), 1053–1079. https://doi.org/10.1002/2014JB011642

Konno, K., & Ohmachi, T. (1998). Ground-motion characteristics estimated from spectral ratio between horizontal and vertical components of microtremor. *Bulletin of the Seismological Society of America*, *88*(1), 228–241.

Lancieri, M., Madariaga, R., & Bonilla, F. (2012). Spectral scaling of the aftershocks of the Tocopilla 2007 earthquake in northern Chile. *Geophysical Journal International*, *189*(1), 469–480. https://doi.org/10.1111/j.1365-246x.2011.05327.x

Li, S., Moreno, M., Bedford, J., Rosenau, M., & Oncken, O. (2015). Revisiting viscoelastic effects on interseismic deformation and locking degree: A case study of the Peru-north Chile subduction zone. *Journal of Geophysical. Research: Solid Earth*, *120*(6), 4522–4538. https://doi.org/10.1002/2015jb011903

Madariaga, R. (1976). Dynamics of an expanding circular fault. *Bulletin of the Seismological Society of America*, *66*(3), 639–666.

Menke, W. (1999). Using waveform similarity to constrain earthquake locations. *Bulletin of the Seismological Society of America*, *89*(4), 1143–1146.

Moreno, M., Li, S., Melnick, D., Bedford, J. R., Baez, J. C., Motagh, M., et al. (2018). Chilean megathrust earthquake recurrence linked to frictional contrast at depth. *Nature Geoscience*, *11*(4), 285–290. https://doi.org/10.1038/s41561-018-0089-5

Moreno, M., Metzger, S., Bedford, J., Hoffmann, F., Li, S., Deng, Z., et al. (2016). Satellitengeodäsie und Erdbebendeformation in der nordchilenischen seismischen lücke. *System Erde*, *6*(2), 36–41.

Mueller, C. S. (1985). Source pulse enhancement by deconvolution of an empirical Green's function. *Geophysical Research Letters*, *12*, 33–36. https://doi.org/10.1029/gl012i001p00033

Münchmeyer, J., Bindi, D., Sippl, C., Leser, U., & Tilmann, F. (2020). Low uncertainty multifeature magnitude estimation with 3-D corrections and boosting tree regression: Application to north Chile. *Geophysical Journal International*, *220*(1), 142–159. https://doi.org/10.1093/gji/ggz416

Pérez, F., & Granger, B. E. (2007). Ipython: A system for interactive scientific computing. *Computing in Science & Engineering*, *9*(3). https://doi.org/10.1109/mcse.2007.53

Prieto, G. A., Shearer, P. M., Vernon, F. L., & Kilb, D. (2004). Earthquake source scaling and self-similarity estimation from stacking *P* and *S* spectra. *Journal of Geophysical Research: Solid Earth*, *109*(B8). https://doi.org/10.1029/2004jb003084

Ruhl, C. J., Abercrombie, R. E., & Smith, K. D. (2017). Spatiotemporal variation of stress drop during the 2008 Mogul, Nevada, earthquake swarm. *Journal of Geophysical Research: Solid Earth*, *122*(10), 8163–8180. https://doi.org/10.1002/2017jb014601

Ruiz, S., Metois, M., Fuenzalida, A., Ruiz, J., Leyton, F., Grandin, R., et al. (2014). Intense foreshocks and a slow slip event preceded the 2014 Iquique Mw 8.1 earthquake. *Science*, *345*(6201), 1165–1169. https://doi.org/10.1126/science.1256074

Sato, T., & Hirasawa, T. (1973). Body wave spectra from propagating shear cracks. *Journal of Physics of the Earth*, *21*(4), 415–431. https://doi.org/10.4294/jpe1952.21.415

Schurr, B., Asch, G., Hainzl, S., Bedford, J., Hoechner, A., Palo, M., et al. (2014). Gradual unlocking of plate boundary controlled initiation of the 2014 Iquique earthquake. *Nature*, *512*(7514), 299. https://doi.org/10.1038/nature13681

Schurr, B., Asch, G., Rosenau, M., Wang, R., Oncken, O., Barrientos, S., et al. (2012). The 2007 m7. 7 Tocopilla northern Chile earthquake sequence: Implications for along-strike and downdip rupture segmentation and megathrust frictional behavior. *Journal of Geophysical Research*, *117*(B5). https://doi.org/10.1029/2011jb009030

Shearer, P. M., Abercrombie, R. E., Trugman, D. T., & Wang, W. (2019). Comparing EGF methods for estimating corner frequency and stress drop from *P* wave spectra. *Journal of Geophysical Research: Solid Earth*, *124*(4), 3966–3986. https://doi.org/10.1029/2018jb016957

Shearer, P. M., Prieto, G. A., & Hauksson, E. (2006). Comprehensive analysis of earthquake source spectra in southern California. *Journal of Geophysical Research: Solid Earth*, *111*(B6). https://doi.org/10.1029/2005jb003979

Sibson, R. H. (1974). Frictional constraints on thrust, wrench and normal faults. *Nature*, *249*(5457), 542–544. https://doi.org/10.1038/249542a0

Sippl, C., Schurr, B., Asch, G., & Kummerow, J. (2018). Seismicity structure of the northern Chile forearcfFrom >100,000 double-difference relocated hypocenters. *Journal of Geophysical Research: Solid Earth*, *123*, 4063. https://doi.org/10.1002/2017JB015384

Tassara, X., & Abercrombie, R. E. (2020). Improved approach for stress drop estimation and its application to an induced earthquake sequence in Oklahoma. *Geophysical Journal International*, *223*(1), 233–253. https://doi.org/10.1093/gji/ggaa316

Trugman, D. T. (2020). Stress-drop and source scaling of the 2019 Ridgecrest, California, earthquake sequence. *Bulletin of the Seismological Society of America*, *110*(4), 1859–1871.

Trugman, D. T., & Shearer, P. M. (2017). Application of an improved spectral decomposition method to examine earthquake source scaling in Southern California. *Journal of Geophysical Research: Solid Earth*, *122*(4), 2890–2910. https://doi.org/10.1002/2017jb013971

Uchide, T., Shearer, P. M., & Imanishi, K. (2014). Stress drop variations among small earthquakes before the 2011 Tohoku-oki, Japan, earthquake and implications for the main shock. *Journal of Geophysical Research: Solid Earth*, *119*(9), 7164–7174. https://doi.org/10.1002/2014jb010943

Venkataraman, A., & Kanamori, H. (2004). Observational constraints on the fracture energy of subduction zone earthquakes. *Journal of Geophysical Research*, *109*(B5). https://doi.org/10.1029/2003jb002549

Vigny, A., Brodsky, E. E., & Axen, G. J. (2007). Evolution of fault-surface roughness with slip. *Geologica*, *35*(3), 283–286. https://doi.org/10.1130/g23235a.1

Virtanen, P., Gommers, R., Oliphant, T. E., Haberland, M., Reddy, T., & Cournapeau, D. (2020). Scipy 1.0: Fundamental algorithms for scientific computing in Python. *Nature Methods*, *17*, 1–12.

Walt, S. v. d., Colbert, S. C., & Varoquaux, G. (2011). The NumPy array: A structure for efficient numerical computation. *Computing in Science & Engineering*, *13*(2), 22–30.

Ye, L., Lay, T., Kanamori, H., & Rivera, L. (2016). Rupture characteristics of major and great (Mw ≥7.0) megathrust earthquakes from 1990 to 2015: 1. Source parameter scaling relationships. *Journal of Geophysical Research: Solid Earth*, *121*(2), 826–844. https://doi.org/10.1002/2015jb012426